

Measurement of Atmospheric Neutrino Oscillations with the ANTARES Neutrino Telescope

S. Adrián-Martínez^a, I. Al Samarai^b, A. Albert^c, M. André^d, M. Anghinolfi^c, G. Anton^f, S. Anvar^g, M. Ardid^a, T. Astraatmadja^{h,1}, J.-J. Aubert^b, B. Baretⁱ, S. Basa^j, V. Bertin^b, S. Biagi^{k,l}, C. Bigongiari^m, C. Bogazzi^h, M. Bou-Cabo^a, B. Bouhouⁱ, M.C. Bouwhuis^h, J. Brunner^b, J. Busto^b, A. Capone^{n,o}, C. Cârloganu^p, J. Carr^b, S. Cecchini^k, Z. Charif^b, Ph. Charvis^q, T. Chiarusi^k, M. Circella^r, R. Coniglione^s, L. Core^b, H. Costantini^b, P. Coyle^b, A. Creusotⁱ, C. Curtil^b, G. De Bonis^{n,o}, M.P. Decowski^h, I. Dekeysers^t, A. Deschamps^q, C. Distefano^s, C. Donzaud^{h,u}, D. Dornic^{b,m}, Q. Dorosti^v, D. Drouhin^c, T. Eberl^f, U. Emanuele^m, A. Enzenhöfer^f, J.-P. Ernenwein^b, S. Escoffier^b, K. Fehn^f, P. Fermani^{n,o}, M. Ferri^a, S. Ferry^w, V. Flaminio^{x,y}, F. Folger^f, U. Fritsch^f, J.-L. Fuda^t, S. Galatà^b, P. Gay^p, K. Geyser^f, G. Giacomelli^{k,l}, V. Giordano^s, A. Gleixner^f, J.P. Gómez-González^m, K. Graf^f, G. Guillard^p, G. Hallewell^b, M. Hamal^z, H. van Haren^{aa}, A.J. Heijboer^h, Y. Hello^q, J.J. Hernández-Rey^m, B. Herold^f, J. Hößl^f, C.C. Hsu^h, M. de Jong^{h,1}, M. Kadler^{ab}, O. Kalekin^f, A. Kappes^{f,2}, U. Katz^f, O. Kavatsyuk^v, P. Kooijman^{h,ac,ad}, C. Kopper^{h,f}, A. Kouchnerⁱ, I. Kreykenbohm^{ab}, V. Kulikovskiy^{ae,e}, R. Lahmann^f, G. Lambard^m, G. Larosa^a, D. Lattuada^s, D. Lefèvre^t, G. Lim^{h,ad}, D. Lo Presti^{af,ag}, H. Loehner^v, S. Loucatos^w, F. Louis^g, S. Mangano^m, M. Marcelinⁱ, A. Margiotta^{k,l}, J.A. Martínez-Mora^a, A. Meli^f, T. Montaruli^{ra,ah}, M. Morganti^{x,3}, L. Moscosp^{i,w,4}, H. Motz^f, M. Neff^f, E. Nezri^j, D. Palioselitis^h, G.E. Pávālaš^{ai}, K. Payet^w, J. Petrovic^h, P. Piattelli^s, V. Popa^{ai}, T. Pradier^{aj}, E. Presani^h, C. Racca^c, C. Reed^h, G. Riccobene^s, C. Richardt^f, R. Richter^f, C. Rivière^b, A. Robert^t, K. Roensch^f, A. Rostovtsev^{ak}, J. Ruiz-Rivas^m, M. Rujoiu^{ai}, G.V. Russo^{af,ag}, D. F. E. Samtleben^h, A. Sánchez-Losa^m, P. Sapienza^s, J. Schmid^f, J. Schnabel^f, F. Schöck^f, J.-P. Schuller^w, F. Schüssler^w, T. Seitz^f, R. Shanidze^f, F. Simeone^{n,o}, A. Spies^f, M. Spurio^{k,l}, J.J.M. Steijger^h, Th. Stolarczyk^w, M. Taiuti^{ca,al}, C. Tamburini^t, A. Trovato^{af}, B. Vallage^w, C. Vallée^b, V. Van Elewyckⁱ, M. Vecchi^b, P. Vernin^w, E. Visser^h, S. Wagner^f, G. Wijnker^h, J. Wilms^{ab}, E. de Wolf^{h,ad}, H. Yepes^m, D. Zaborov^{ak}, J.D. Zornoza^m, J. Zúñiga^m

^aInstitut d'Investigació per a la Gestió Integrada de les Zones Costaneres (IGIC) - Universitat Politècnica de València. C/Paraním 1, 46730 Gandia, Spain.

^bCPPM, Aix-Marseille Université, CNRS/IN2P3, Marseille, France

^cGRPHE - Institut universitaire de technologie de Colmar, 34 rue du Grillenbreit BP 50568 - 68008 Colmar, France

^dTechnical University of Catalonia, Laboratory of Applied Bioacoustics, Rambla Exposició, 08800 Vilanova i la Geltrú, Barcelona, Spain

^eINFN - Sezione di Genova, Via Dodecaneso 33, 16146 Genova, Italy

^fFriedrich-Alexander-Universität Erlangen-Nürnberg, Erlangen Centre for Astroparticle Physics, Erwin-Rommel-Str. 1, 91058 Erlangen, Germany

^gDirection des Sciences de la Matière - Institut de recherche sur les lois fondamentales de l'Univers - Service d'Electronique des Détecteurs et d'Informatique, CEA Saclay, 91191 Gif-sur-Yvette Cedex, France

^hNikhef, Science Park, Amsterdam, The Netherlands

ⁱAPC - Laboratoire AstroParticule et Cosmologie, UMR 7164 (CNRS, Université Paris 7 Diderot, CEA, Observatoire de Paris) 10, rue Alice Domon et Léonie Duquet 75205 Paris Cedex 13, France

^jLAM - Laboratoire d'Astrophysique de Marseille, Pôle de l'Étoile Site de Château-Gombert, rue Frédéric Joliot-Curie 38, 13388 Marseille Cedex 13, France

^kINFN - Sezione di Bologna, Viale Bertini-Pichat 6/2, 40127 Bologna, Italy

^lDipartimento di Fisica dell'Università, Viale Bertini Pichat 6/2, 40127 Bologna, Italy

^mIFIC - Instituto de Física Corpuscular, Edificios Investigación de Paterna, CSIC - Universitat de València, Apdo. de Correos 22085, 46071 Valencia, Spain

ⁿINFN - Sezione di Roma, P.le Aldo Moro 2, 00185 Roma, Italy

^oDipartimento di Fisica dell'Università La Sapienza, P.le Aldo Moro 2, 00185 Roma, Italy

^pClermont Université, Université Blaise Pascal, CNRS/IN2P3, Laboratoire de Physique Corpusculaire, BP 10448, 63000 Clermont-Ferrand, France

^qGéozur - Université de Nice Sophia-Antipolis, CNRS/INSU, IRD, Observatoire de la Côte d'Azur and Université Pierre et Marie Curie, BP 48, 06235 Villefranche-sur-mer, France

^rINFN - Sezione di Bari, Via E. Orabona 4, 70126 Bari, Italy

^sINFN - Laboratori Nazionali del Sud (LNS), Via S. Sofia 62, 95123 Catania, Italy

^tCOM - Centre d'Océanologie de Marseille, CNRS/INSU et Université de la Méditerranée, 163 Avenue de Luminy, Case 901, 13288 Marseille Cedex 9, France

^uUniv Paris-Sud, 91405 Orsay Cedex, France

^vKernfysisch Versneller Instituut (KVI), University of Groningen, Zernikelaan 25, 9747 AA Groningen, The Netherlands

^wDirection des Sciences de la Matière - Institut de recherche sur les lois fondamentales de l'Univers - Service de Physique des Particules, CEA Saclay, 91191 Gif-sur-Yvette Cedex, France

^xINFN - Sezione di Pisa, Largo B. Pontecorvo 3, 56127 Pisa, Italy

^yDipartimento di Fisica dell'Università, Largo B. Pontecorvo 3, 56127 Pisa, Italy

^zUniversity Mohammed I, Laboratory of Physics of Matter and Radiations, B.P.717, Oujda 6000, Morocco

^{aa}Royal Netherlands Institute for Sea Research (NIOZ), Landsdiep 4, 1797 SZ 't Horntje (Texel), The Netherlands

^{ab}Dr. Reemis-Sternwarte and ECAP, Universität Erlangen-Nürnberg, Sternwartstr. 7, 96049 Bamberg, Germany

^{ac}Universiteit Utrecht, Faculteit Betawetenschappen, Princetonplein 5, 3584 CC Utrecht, The Netherlands

^{ad}Universiteit van Amsterdam, Instituut voor Hoge-Energie Fysica, Science Park 105, 1098 XG Amsterdam, The Netherlands

^{ae}Moscow State University, Skobeltsyn Institute of Nuclear Physics, Leninskie gory, 119991 Moscow, Russia

^{af}INFN - Sezione di Catania, Viale Andrea Doria 6, 95125 Catania, Italy

^{ag}Dipartimento di Fisica ed Astronomia dell'Università, Viale Andrea Doria 6, 95125 Catania, Italy

^{ah}Département de Physique Nucléaire et Corpusculaire, Université de Genève, 1211, Geneva, Switzerland

^{ai}Institute for Space Sciences, R-77125 Bucharest, Măgurele, Romania

^{aj}IPHC-Institut Pluridisciplinaire Hubert Curien - Université de Strasbourg et CNRS/IN2P3 23 rue du Loess, BP 28, 67037 Strasbourg Cedex 2, France

Abstract

The data taken with the ANTARES neutrino telescope from 2007 to 2010, a total live time of 863 days, are used to measure the oscillation parameters of atmospheric neutrinos. Muon tracks are reconstructed with energies as low as 20 GeV. Neutrino oscillations will cause a suppression of vertical upgoing muon neutrinos of such energies crossing the Earth. The parameters determining the oscillation of atmospheric neutrinos are extracted by fitting the event rate as a function of the ratio of the estimated neutrino energy and reconstructed flight path through the Earth. Measurement contours of the oscillation parameters in a two-flavour approximation are derived. Assuming maximal mixing, a mass difference of $\Delta m_{32}^2 = (3.1 \pm 0.9) \cdot 10^{-3} \text{ eV}^2$ is obtained, in good agreement with the world average value.

Keywords: neutrino oscillations, neutrino telescope, ANTARES

1. Introduction

A measurement of the quantum mechanical phenomenon of neutrino oscillations provides important information on the mass differences of the neutrino mass eigenstates and their mixing angles. The effect was discovered by Super-Kamiokande [1] on neutrinos produced in the Earth atmosphere. In this paper, the first observation of neutrino oscillations by a high energy neutrino telescope is presented. As this measurement addresses a higher neutrino energy range, the analysis presented here is complementary to previous measurements. In particular, the selection procedure for ν_μ events, on which the oscillation parameters are measured, is different with respect to a similar analysis at lower energies. Whereas the separation of ν_μ charged current events from ν_e and neutral current events becomes much easier, handling the background from misreconstructed downgoing muons is more challenging (see Section 6).

The main goal of the ANTARES deep sea neutrino telescope [2] is the observation of high energy neutrinos from non-terrestrial sources. The telescope is optimised for the detection of Cherenkov light induced by the passage of upgoing muons produced in charged current interactions of neutrinos at TeV energies, for which the muon can traverse completely the equipped detector volume. At lower neutrino energies, both the cross section and the muon range are smaller resulting in a decrease of the detection efficiency. For the analysis presented here, the lowest energies of detectable muons from neutrino interactions are about 20 GeV. For upgoing atmospheric neutrinos which traverse the Earth, this threshold is low enough for the observed flux of ν_μ induced events to be significantly suppressed by neutrino oscillations. By studying the observed upgoing muon rate as a function of the ratio of the reconstructed muon energy and zenith angle, constraints on the atmospheric neutrino oscillation parameters are derived.

The paper is organised as follows: in Section 2 the phenomenology of atmospheric neutrino oscillations is introduced and the method used to extract the oscillation parameters is discussed. The ANTARES telescope is described in Section 3. The data set and the Monte Carlo simulations are explained in Section 4. The methods to reconstruct the neutrino direction and energy are discussed in Section 5 followed by details of the event selection in Section 6. A discussion on systematic uncertainties is given in Section 7 and the final results are presented in Section 8.

¹Also at University of Leiden, the Netherlands

²On leave of absence at the Humboldt-Universität zu Berlin

³Also at Accademia Navale de Livorno, Livorno, Italy

⁴Deceased

2. Neutrino Oscillations

The survival probability of atmospheric ν_μ in the framework of three flavour mixing is given as

$$P(\nu_\mu \rightarrow \nu_\mu) = 1 - 4|U_{\mu 1}|^2|U_{\mu 2}|^2 \sin^2\left(\frac{1.27\Delta m_{21}^2 L}{E_\nu}\right) - 4|U_{\mu 1}|^2|U_{\mu 3}|^2 \sin^2\left(\frac{1.27\Delta m_{31}^2 L}{E_\nu}\right) - 4|U_{\mu 2}|^2|U_{\mu 3}|^2 \sin^2\left(\frac{1.27\Delta m_{32}^2 L}{E_\nu}\right) \quad (1)$$

where L is the travel path (in km) of the neutrino through the Earth and E_ν , its energy (in GeV). U_{ai} is the 3×3 PMNS-matrix which describes the mixing between flavour eigenstates ν_e, ν_μ, ν_τ and mass eigenstates ν_1, ν_2, ν_3 and $\Delta m_{ij}^2 = |m_i^2 - m_j^2|$ (in eV^2) is the absolute difference of the squares of the masses of the corresponding neutrino mass eigenstates. The present analysis is restricted to $L < 12800$ km and $E_\nu > 20$ GeV, for which the term $\sin^2(1.27\Delta m_{21}^2 L/E_\nu)$ does not exceed $3.7 \cdot 10^{-3}$ when using Δm_{21}^2 from [3]. This term can safely be ignored as well as differences between Δm_{31}^2 and Δm_{32}^2 and Equation 1 simplifies to

$$P(\nu_\mu \rightarrow \nu_\mu) = 1 - 4(1 - |U_{\mu 3}|^2)|U_{\mu 3}|^2 \sin^2\left(\frac{1.27\Delta m_{32}^2 L}{E_\nu}\right) \quad (2)$$

Results could in principle be extracted in terms of $|U_{\mu 3}|^2$ and Δm_{32}^2 which are the two oscillation parameters in Equation 2. To maintain compatibility with earlier results, a mixing angle $\sin^2 2\theta_{23} = |U_{\mu 3}|^2$ is defined, ignoring the 2.4% deviation from 1 of $\cos^2 \theta_{13} = 0.976$ [4]. This leads to the usual two-flavour description

$$P(\nu_\mu \rightarrow \nu_\mu) = 1 - \sin^2 2\theta_{23} \sin^2\left(\frac{1.27\Delta m_{32}^2 L}{E_\nu}\right) = 1 - \sin^2 2\theta_{23} \sin^2\left(\frac{16200 \Delta m_{32}^2 \cos \Theta}{E_\nu}\right). \quad (3)$$

For upgoing tracks L is in good approximation related to the zenith angle Θ by $L = D \cdot \cos \Theta$ where D is the Earth diameter. The transition probability, P , depends now on only two oscillation parameters, Δm_{32}^2 and $\sin^2 2\theta_{23}$, which determine the behaviour for the atmospheric neutrino oscillations.

With $\Delta m_{32}^2 = 2.43 \cdot 10^{-3} \text{ eV}^2$ and $\sin^2 2\theta_{23} = 1$ from [3] one expects the first oscillation maximum, *i.e.* $P(\nu_\mu \rightarrow \nu_\mu) = 0$ for vertical upgoing neutrinos ($\cos \Theta = 1$) of $E_\nu = 24$ GeV. Muons induced by 24 GeV neutrinos can travel up to 120 m in sea water.

The observed number of events in bin i , N_i , of a given variable can be compared to the number MC_i of expected Monte Carlo events in the same channel

$$MC_i = \mu_i + \sum_k \left[1 - \sin^2 2\theta_{23} \sin^2\left(\frac{16200 \Delta m_{32}^2 \cos \Theta_{ik}}{E_{\nu,ik}}\right) \right] \quad (4)$$

where μ_i is the number of the background atmospheric muon events in channel i and the sum gives the number of atmospheric neutrino events in channel i weighted by the event dependent oscillation probability from Equation 3. As the oscillation probability $P(\nu_\mu \rightarrow \nu_\mu)$ depends on $E_\nu/\cos \Theta$, the natural choice for a variable in which the channel i can be defined is the ratio between a quantity which depends on the neutrino energy and the reconstructed zenith angle, Θ_R . As explained in Section 5, the energy-dependent variable is the observed muon range in the detector. The oscillation parameters are extracted by a χ^2 minimisation which is detailed in Section 7.

3. The ANTARES Detector

A detailed description of the ANTARES detector can be found in [2]. The detector consists of 12 lines, equipped with photosensors, and a junction box which distributes the power and clock synchronization signals to the lines and collects the data. The junction box is connected to the shore by a 42 km electro-optical cable. The length of the detection lines is 450 m, of which the lowest 100 m are not instrumented. Their horizontal separation is about 65 m and they are arranged to form a regular octagon on the sea floor. They are connected to the junction box with the help of a submarine using wet-mateable connectors. Each line comprises 25 storeys each separated by a vertical distance of 14.5 m. The lines are kept taut by a buoy at the top of the line and an anchor on the seabed. The movement of the

line elements due to the sea currents is continuously measured by an acoustic calibration system with an accuracy of 10 cm [5].

Each storey contains three 45° downward-looking 10” photomultiplier tubes (PMT) inside pressure resistant glass spheres - the optical modules [6]. Some of the storeys contain supplementary calibration equipment such as acoustic hydrophones or optical beacons [7].

The signals of each photomultiplier are readout by two ASICs. The charges and arrival times of the PMT signals are digitised and stored for transfer to the shore station [8]. The time stamps are synchronised by a clock signal which is sent at regular intervals from the shore to all electronic cards. The overall time calibration is better than 0.5 ns [9]. Therefore the time resolution of the signal pulses is limited by the transit time spread of the photomultipliers ($\sigma \sim 1.3$ ns) [10] and by chromatic dispersion for distant light sources. All data are sent to the shore station. With the observed optical background rate of 70 kHz per PMT at the single photon level this produces a data flow of several Gbit/s to the shore. In the shore station a PC farm performs a data filtering to reduce the data rate by at least a factor of 100 [11]. Several trigger algorithms are applied depending on the requested physics channel and on the observed optical noise.

4. Data and Simulations

The present analysis is based on data taken with the ANTARES detector between March 2007 and December 2010. Until December 2007 ANTARES operated in a 5-line configuration, followed by several months of operation with 10 installed detector lines. The detector construction was completed in May 2008. All physics runs taken under normal conditions have been used. The events selected by two tight trigger conditions are used [2]. The analysed sample consists of 293 million triggers, dominated by atmospheric muons, corresponding to a detector live time of 863 days.

Downgoing atmospheric muons were simulated with the program MUPAGE [12, 13] which provides parametrised muon bundles at the detector. Upgoing neutrinos were simulated according to the parametrisation of the atmospheric ν_μ flux from [14] in the energy range from 10 GeV to 10 PeV. The Cherenkov light, produced inside or in the vicinity of the detector instrumented volume, was propagated taking into account light absorption and scattering in sea water [15]. The angular acceptance, quantum efficiency and other characteristics of the PMTs were taken from [6] and the overall geometry corresponded to the layout of the ANTARES detector [2]. The optical noise was simulated from counting rates observed in the data. At the same time, the definition of active and inactive channels has been applied from data runs as well. The generated statistics corresponds to an equivalent observation time of 100 years for atmospheric neutrinos and ten months for atmospheric muons.

5. Reconstruction

The algorithm used for the muon track reconstruction is described in [16]. It assumes a simplified detector geometry composed of straight vertical detection lines. The method combines a strict selection of direct Cherenkov photon hits which are grouped around “hot spots” at each detector line with a χ^2 -like fitting procedure. A hot spot corresponds to a signal of at least 4 photoelectrons seen on two adjacent storeys of the same detector line within a narrow time window of less than 100 ns. Only hits on detector lines with such a hot spot are used in the track fitting. If the selected hits occur only on one detector line, a single-line fit is performed. No azimuth angle is determined in this case due to the rotational symmetry of the problem. This does not affect the present measurement, as the oscillation probability does not depend on the azimuth angle (see Equation 3). If selected hits occur instead on several detector lines, a multi-line fit is performed which provides both the zenith and azimuth angles of the track. The inclusion of single-line events is a special feature of the reconstruction method and allows to significantly lower the energy threshold of the final atmospheric neutrino sample. Whereas for multi-line events the threshold energy of the final neutrino sample is about 50 GeV due to the 65 m horizontal gap between lines, single-line events are reconstructed down to 20 GeV for nearly vertical tracks, accessing events with E_ν/L values close to the first oscillation maximum.

The neutrino energy is estimated from the observed muon range in the detector. The selected hits are sorted according to their vertical position, z . The z -coordinates of the uppermost and lowermost hits, z_{max} and z_{min} , together

with the reconstructed zenith angle, Θ_R , allow to define an approximate muon range

$$S = (z_{max} - z_{min}) / \cos \Theta_R. \quad (5)$$

When considering the geometry of the Cherenkov light cone, Equation 5 is exact only for strictly vertical tracks. It has been verified that the use of a more sophisticated range definition does not improve the precision of the measurement for the oscillation parameters. S is used to estimate the muon energy by taking into account the ionisation energy loss of 0.2 GeV/m for minimum ionising muons in sea water [3]

$$E_R = S \cdot 0.2 \text{ GeV/m}. \quad (6)$$

The derived energy from the visible muon range in the detector can be considered as a lower limit of the actual neutrino energy. The presence of a hadronic shower at the neutrino vertex is ignored, as well as the fact that the muon might leave or enter the detector, making only a fraction of its actual range available for measurement. The normalised difference between the true neutrino energy, E_ν , and E_R is shown in Figure 1 for all selected simulated events (see Section 6) with $E_\nu < 100$ GeV. The mean value of 0.45 illustrates the fact that E_R measures on average about half of the neutrino energy. The RMS of the distribution is 0.22.

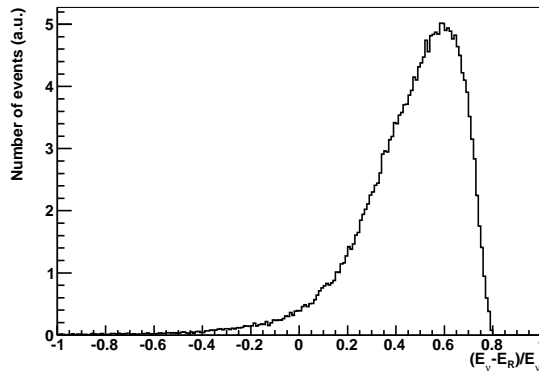


Figure 1: Difference between the true neutrino energy, E_ν , and E_R normalised by E_ν for low energy events ($E_\nu < 100$ GeV) from the final event sample of Section 6.

6. Event Selection

Downgoing atmospheric muons dominate the ANTARES event sample on the trigger level as illustrated in Table 1. Neutrinos contribute less than 10^{-4} here. In principle a simple cut in the reconstructed zenith angle should be enough to separate both classes. But as seen from Table 1, this is not sufficient. Atmospheric muons are often seen as bundles and they can be accompanied by hard stochastic processes such as bremsstrahlung. Both effects complicate their correct reconstruction and a certain fraction of downgoing atmospheric muon events are misreconstructed as upgoing. Some cuts on the quality of the reconstructed tracks are needed to reduce this contamination and derive reliably neutrino oscillation parameters from the data set. The goodness of the track fit is measured by the “normalised fit quality” as introduced in [16], a quantity equivalent to a χ^2 per number of degrees of freedom (NDF). The selection cuts, which are described below, have been obtained from a blind analysis. The single-line data sample has been kept blind, thereby masking a possible oscillation signature.

For the multi-line selection, only events which have hits on more than 5 storeys are kept to allow a non-degenerate track fit. Further, the fit must not converge on a physical boundary of any of the fit parameters. As the contamination of misreconstructed atmospheric muons is particularly strong close to the horizon, a further condition, $\cos \Theta_R > 0.15$, is imposed, *i.e.* tracks closer than 9° to the horizon are excluded.

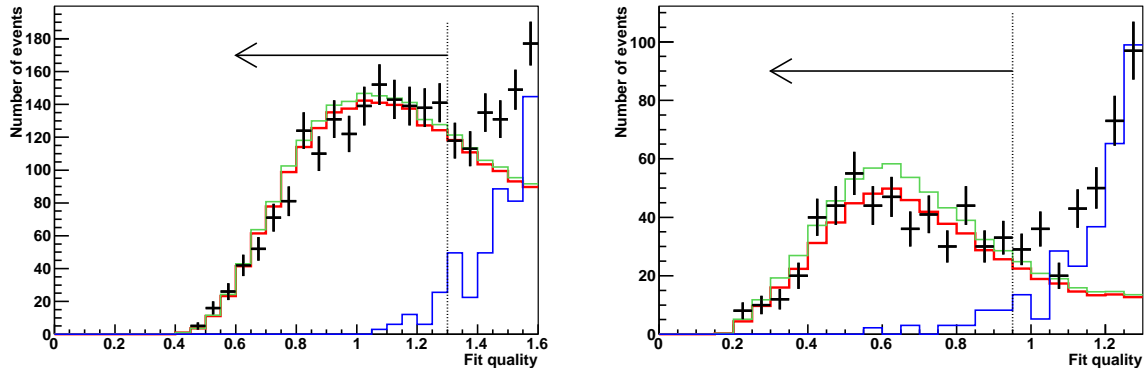


Figure 2: Normalised fit quality of the final multi-line (left) and single-line (right) samples. Data with statistical errors (black) are compared to simulations from atmospheric neutrinos with oscillations assuming parameters from [3] (red) and without oscillations (green) and atmospheric muons (blue). For a fit quality larger than 1.6 (multi-line) or 1.3 (single-line) the misreconstructed atmospheric muons dominate. The arrows indicate the chosen regions.

The distribution of the normalised track fit quality of the resulting multi-line event sample for data and simulations is shown in Figure 2 (left). The neutrino Monte Carlo samples are scaled down by an overall normalisation factor $r = 0.86$ as obtained from the fit (see Section 8). This is well within the uncertainty of the atmospheric neutrino flux model [17]. Figure 2 (left) shows that a cut on the normalised fit quality allows to cleanly separate the upgoing neutrinos from the downgoing muons. In order to have a contamination of misreconstructed atmospheric muons below 5%, a cut value of 1.3 is chosen.

For the single-line selection, events which have hits on more than 7 storeys are kept. This yields a minimal track length for a vertical upgoing muon of about 100 m, which can be produced by a muon of 20 GeV. Further cuts are identical to the multi-line selection.

The distribution of the normalised track fit quality of the resulting single-line event sample for data and simulations is shown in Figure 2 (right). The neutrino Monte Carlo samples are again scaled down by a factor $r = 0.86$. Figure 2 (right) shows that also for this data set a cut on the normalised fit quality allows to cleanly separate the downgoing muons from the upgoing neutrinos. In order to have a contamination of misreconstructed atmospheric muons below 5%, a cut value of 0.95 is chosen.

	Multi-line			Single-line		
	Data	ν MC	μ MC	Data	ν MC	μ MC
All	$1.42 \cdot 10^8$	8755	$1.23 \cdot 10^8$	$1.51 \cdot 10^8$	8242	$1.10 \cdot 10^8$
Nstorey > N_{cut}	$1.33 \cdot 10^8$	8248	$1.18 \cdot 10^8$	$4.44 \cdot 10^7$	1260	$3.03 \cdot 10^7$
Fit boundary	$1.32 \cdot 10^8$	8150	$1.17 \cdot 10^8$	$4.31 \cdot 10^7$	1242	$2.93 \cdot 10^7$
$\cos \Theta_R > 0.15$	$2.74 \cdot 10^6$	5512	$1.84 \cdot 10^6$	$7.97 \cdot 10^5$	1116	$6.96 \cdot 10^5$
Fit quality cut	1632 ± 40	1971 ± 6 1910 ± 6	52 ± 12	494 ± 22	651 ± 3 557 ± 3	28 ± 9

Table 1: Event reduction due to the cuts used. Statistical errors are given for the final data set. The effect of oscillations with parameters from [3] is taken into account only for the values given in the very last row.

The effect of the different selection cuts in the two channels is detailed in Table 1 for data and the Monte Carlo sets. Satisfactory agreement between data and Monte Carlo numbers is observed at all cut levels.

Events from ν_e charged current (CC) interactions as well as neutral current (NC) interactions produce cascade-like event topologies. The spatial extension of these cascades, which are composed of the hadronic and electromagnetic

showers at the neutrino interaction vertex, does not exceed more than a few meters. This is in contrast to the lowest energetic selected muons, which have still a range of at least 100 m in sea water and therefore a distinct topology. The above described selection cuts, tuned to suppress the atmospheric muon background, reduce efficiently also the contribution from ν_μ NC and ν_e interactions. Their contribution to the final event sample is estimated to be less than one event in the multi-line channel and 6 events in the single-line channel. Both numbers are significantly smaller than the residual background contribution from atmospheric muons.

The zenith angle of the final neutrino sample is reconstructed with a precision of 0.8° for multi-line events and 3.0° for single-line events (median of the angular error distribution with respect to the true neutrino direction). The

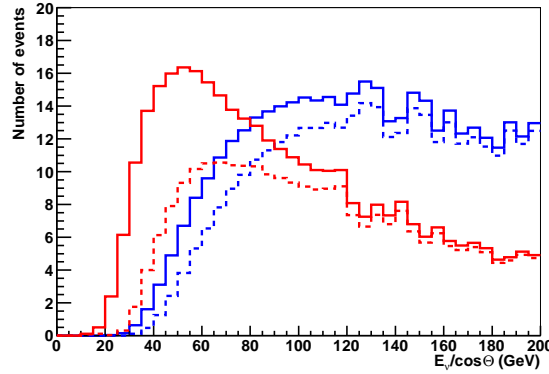


Figure 3: Distribution of $E_\nu / \cos \Theta$ for the selected events of the atmospheric neutrino simulation. The solid lines are without neutrino oscillations, the dashed lines include oscillations assuming the best fit values reported in [3]. The red histograms indicate the contribution of the single-line sample, in blue the multi-line events.

distribution in $E_\nu / \cos \Theta$ for the simulated selected atmospheric neutrino samples is shown in Figure 3. The expected event numbers are shown for the actual detector live time of 863 days. The effect of neutrino oscillations is seen by comparing the Monte Carlo curves with and without oscillations. The importance of the inclusion of the single-line events is evident. The expected deficit due to neutrino oscillations for $E_\nu / \cos \Theta < 200$ GeV amounts to 143 events, the majority of which (91 events) are in the single-line sample. These oscillated events are mainly converted into ν_τ and might produce muons by a ν_τ CC interaction followed by a decay $\tau^- \rightarrow \mu^- \bar{\nu}_\mu \nu_\tau$ (or charge conjugate). To estimate the appearance of muons from ν_τ interactions in the final event sample, the energy dependent cross section ratio $\sigma(\nu_\tau CC) / \sigma(\nu_\mu CC)$, about 0.5 for $E_\nu = 25$ GeV, the 17% branching ratio of the muonic τ -decay and the soft energy spectrum of the resulting muons have to be considered. It is found that the expected deficit due to oscillations is reduced by less than 5 events.

7. Systematic Uncertainties

Systematic uncertainties lead to a correlated distortion of the $E_R / \cos \Theta_R$ distribution. They are implemented as pull factors in the χ^2 function to be minimised:

$$\chi^2 = \sum_i \left[N_i - (1 + \epsilon)MC_i^{1L} - (1 + \eta)MC_i^{ML} \right]^2 / \sigma_i^2 + (\epsilon - \eta)^2 / \sigma_R^2. \quad (7)$$

The sum extends over the bins in $E_R / \cos \Theta_R$ with N_i the observed number of events in bin i whereas MC_i^{1L} and MC_i^{ML} denote the expected event numbers from simulations in the single-line and multi-line channel respectively and σ_i is the corresponding statistical error of bin i . The simulated event numbers depend on the oscillation parameters according to Equation 4. The quantities ϵ and η are two pull factors which allow to renormalise the two channels. The variations of ϵ and η are constrained by σ_R , which is introduced below.

A large class of uncertainties modify the overall normalisation, *i.e.* they act on ϵ and η in the same way. The normalisation of the neutrino flux model as well as the uncertainty on the absolute neutrino detection efficiency of the ANTARES detector fall into this class. Equation 7 does not constrain such uncertainties, as indicated by the absence of terms such as $\epsilon^2/\sigma_\epsilon^2$ or η^2/σ_η^2 , *i.e.* the relative overall normalisation between data and simulations is left totally free in this analysis.

A second class of uncertainties might change the shape of the $E_R/\cos\Theta_R$ distribution. Single-line events have typically lower $E_\nu/\cos\Theta$ values (and thus correspondingly lower observed $E_R/\cos\Theta_R$ values) than multi-line events (see Figure 3). A change in the ratio of the total number of events in each sample, $R_0 = N^{1L}/N^{ML}$, would therefore reflect a shape change of the $E_R/\cos\Theta_R$ distribution. In terms of the pull factors this can be written as $R(\epsilon, \eta) = R_0(1 + \epsilon)/(1 + \eta) \approx R_0(1 + \epsilon - \eta)$. Therefore $R(\epsilon, \eta)$ varies with $\epsilon - \eta$ if both pull factors are small.

Several simulations have been performed with modified input parameters which may affect in a slightly different manner vertical and horizontal events (thereby acting on $\cos\Theta_R$) as well as low and high energy events [18]. The average quantum efficiency of the phototubes was changed by $\pm 10\%$ as well as their angular acceptance. The water absorption length of sea water was also varied by $\pm 10\%$. Further, the cuts in the normalised fit quality were varied in two steps of 0.05 around the chosen values thereby testing the stability of the analysis procedure. The spectral index of the atmospheric neutrino flux was varied by ± 0.03 as suggested in [19]. As a result a set of values of R was derived. It was observed that R remains stable within 5% of its original value, R_0 . This value $\sigma_R = 0.05$ is used in Equation 7 to constrain relative variations of ϵ and η . This accounts for the maximal variation of the shape of the $E_R/\cos\Theta_R$ distribution due to the considered systematic effects.

8. Results

After applying the cuts defined in Section 6 the final event numbers obtained are given in Table 1. Figure 4 (left) shows the resulting $E_R/\cos\Theta_R$ distribution for data and simulations. Figure 4 (right) shows the fraction of measured and simulated events with respect to the non-oscillation Monte Carlo hypothesis and indicates a clear event deficit for $E_R/\cos\Theta_R < 60$ GeV, as expected assuming atmospheric neutrino oscillations. Restricting the χ^2 minimisation to

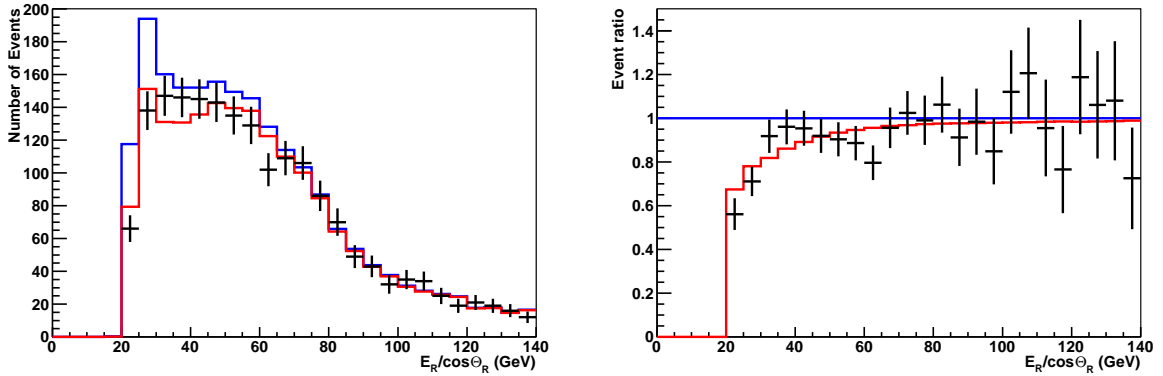


Figure 4: **Left:** Distribution of $E_R/\cos\Theta_R$ for selected events. Black crosses are data with statistical uncertainties, whereas the blue histogram shows simulations of atmospheric neutrinos without neutrino oscillations (scaled down by a factor 0.86) plus the residual background from atmospheric muons. The red histogram shows the result of the fit. **Right:** The fraction of events with respect to the non-oscillation hypothesis. Same color code as for the left figure.

parameters in the physically allowed region yields the red curve of Figure 4 with $\Delta m_{32}^2 = 3.1 \cdot 10^{-3} \text{eV}^2$ and $\sin^2 2\theta_{23} = 1.00$. The corresponding pull factors are $\epsilon = -0.138$ and $\eta = -0.142$. This is used as an overall normalisation parameter $r = 0.86$ in Figures 2 and 4. The fit is performed in 25 bins: the 24 bins shown in Figure 4 plus one overflow bin which contains 299 events with $E_R/\cos\Theta_R > 140$ GeV. The fit yields $\chi^2/\text{NDF} = 17.1/21$. When imposing the world average oscillation parameters, $\Delta m_{32}^2 = 2.43 \cdot 10^{-3} \text{eV}^2$ and $\sin^2 2\theta_{23} = 1$ from [3], $\chi^2/\text{NDF} = 18.4/21$ is found.

For the non-oscillation hypothesis, *i.e.* $\sin^2 2\theta_{23} = 0$, $\chi^2/\text{NDF} = 31.1/23$ is obtained. The pull factors in this case are $\epsilon = -0.302$ and $\eta = -0.196$. The event deficit in the single-line channel is seen here as ϵ becoming lower than η . Requiring in addition $\epsilon = \eta$ the χ^2 increases further to $\chi^2/\text{NDF} = 40.0/24$, which has a probability of only 2.1%.

This measurement is converted into contours of the oscillation parameters and is shown in Figure 5. With 68%

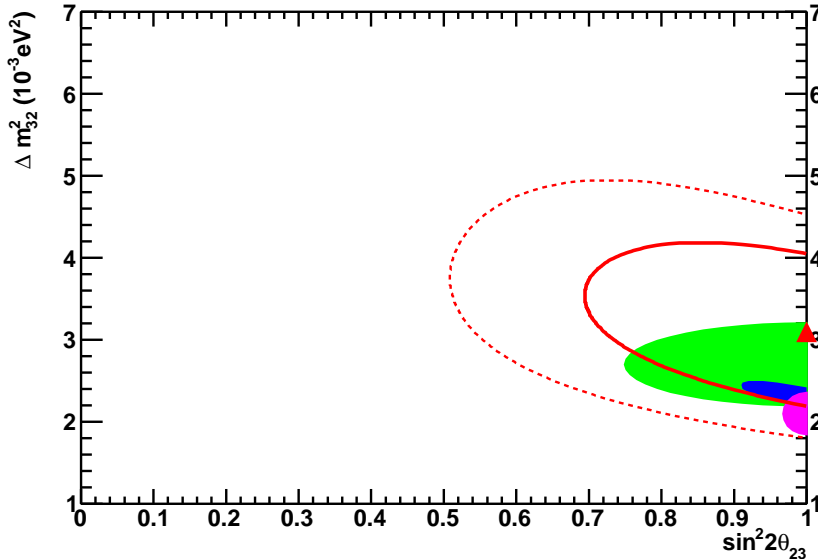


Figure 5: 68% and 90% C.L. contours (solid and dashed red lines) of the neutrino oscillation parameters as derived from the fit of the $E_R/\cos\Theta_R$ distribution. The best fit point is indicated by the triangle. The solid filled regions show results at 68% C.L. from K2K [20] (green), MINOS [21] (blue) and Super-Kamiokande [22] (magenta) for comparison.

C.L. $\sin^2 2\theta_{23} > 0.70$ is found and Δm_{32}^2 is constrained to values in the range $[2.2, 4.2] \cdot 10^{-3} \text{eV}^2$. If maximal mixing is imposed ($\sin^2 2\theta_{23} = 1$), the obtained range of Δm_{32}^2 is

$$\Delta m_{32}^2 = (3.1 \pm 0.9) \cdot 10^{-3} \text{eV}^2. \quad (8)$$

The results are in agreement with other measurements from K2K [20], MINOS [21] and Super-Kamiokande [22].

9. Conclusions

Based on data taken by the ANTARES neutrino telescope from 2007 to 2010, constraints on the neutrino oscillation parameters $\sin^2 2\theta_{23}$ and Δm_{32}^2 have been derived. If maximal mixing is assumed, a value $\Delta m_{32}^2 = (3.1 \pm 0.9) \cdot 10^{-3} \text{eV}^2$ is obtained. The result agrees well with current world data and demonstrates a good understanding of the performance of the ANTARES telescope at its lowest accessible energies. It is the first such measurement by a high energy neutrino telescope and underlines the potential of future low energy extensions of the existing neutrino telescopes for such physics.

10. Acknowledgements

The authors acknowledge the financial support of the funding agencies: Centre National de la Recherche Scientifique (CNRS), Commissariat à l'énergie atomique et aux énergies alternatives (CEA), Commission Européenne (FEDER fund and Marie Curie Program), Région Alsace (contrat CPER), Région Provence-Alpes-Côte d'Azur, Département du Var and Ville de La Seyne-sur-Mer, France; Bundesministerium für Bildung und Forschung (BMBF), Germany; Istituto Nazionale di Fisica Nucleare (INFN), Italy; Stichting voor Fundamenteel Onderzoek der Materie

(FOM), Nederlandse organisatie voor Wetenschappelijk Onderzoek (NWO), the Netherlands; Council of the President of the Russian Federation for young scientists and leading scientific schools supporting grants, Russia; National Authority for Scientific Research (ANCS - UEFISCDI), Romania; Ministerio de Ciencia e Innovación (MICINN), Prometeo of Generalitat Valenciana and MultiDark, Spain; Agence de l'Oriental and CNRST, Morocco. We also acknowledge the technical support of Ifremer, AIM and Foselev Marine for the sea operation and the CC-IN2P3 for the computing facilities.

References

- [1] Y. Fukuda *et al.* [Super-Kamiokande Coll.], *Phys. Rev. Lett.* **81** (1998) 1562.
- [2] M. Ageron *et al.*, [ANTARES Coll.], *Nucl. Instrum. Meth.* **A656** (2011) 11.
- [3] K. Nakamura *et al.* [Particle Data Group], *J. Phys.* **G37** (2010) 075021.
- [4] F. P. An *et al.*, [Daya-Bay Coll.], *Phys. Rev. Lett.* **108** (2012) 171803.
- [5] S. Adrian-Martinez *et al.*, [ANTARES Coll.], arXiv:1202.3894 (2012).
- [6] P. Amram *et al.*, [ANTARES Coll.], *Nucl. Instrum. Meth.* **A484** (2002) 369.
- [7] M. Ageron *et al.*, [ANTARES Coll.], *Nucl. Instrum. Meth.* **A578** (2007) 498.
- [8] J. A. Aguilar *et al.*, [ANTARES Coll.], *Nucl. Instrum. Meth.* **A622** (2010) 59.
- [9] J. A. Aguilar *et al.*, [ANTARES Coll.], *Astropart. Phys.* **34** (2011) 539.
- [10] J. A. Aguilar *et al.*, [ANTARES Coll.], *Nucl. Instrum. Meth.* **A555** (2005) 132.
- [11] J. A. Aguilar *et al.*, [ANTARES Coll.], *Nucl. Instrum. Meth.* **A570** (2007) 107.
- [12] G. Carminati *et al.*, *Comput. Phys. Commun.* **179** (2008) 915.
- [13] Y. Becherini *et al.*, *Astropart. Phys.* **25** (2006) 1.
- [14] G. Barr, *et al.*, *Phys. Rev.* **D39** (1989) 3532; V. Agrawal *et al.*, *Phys. Rev.* **D53** (1996) 1314.
- [15] J. A. Aguilar *et al.*, [ANTARES Coll.], *Astropart. Phys.* **23** (2005) 131.
- [16] J. A. Aguilar *et al.*, [ANTARES Coll.], *Astropart. Phys.* **34** (2011) 652.
- [17] G.D. Barr, T.K. Gaisser, S. Robbins and T. Stanev, *Phys. Rev.* **D74** (2006) 094009.
- [18] J. A. Aguilar *et al.*, [ANTARES Coll.], *Astropart. Phys.* **34** (2010) 179.
- [19] R. Abbasi *et al.*, [IceCube Coll.], *Phys. Rev.* **D84** (2011) 082001.
- [20] M. H. Ahn *et al.*, [K2K Coll.], *Phys. Rev.* **D74** (2006) 072003.
- [21] P. Adamson *et al.*, [MINOS Coll.], *Phys. Rev. Lett.* **106** (2011) 181801.
- [22] K. Abe *et al.*, [Super-Kamiokande Coll.], *Phys. Rev. Lett.* **107** (2011) 241801.